ACS APPLIED MATERIALS & INTERFACES

www.acsami.org Research Article

Chiral Magneto-Optical Properties of Supra-Assembled Fe_3O_4 Nanoparticles

Qysar Maqbool,[⊥] Arum Jung,[⊥] Sojeong Won, Jinhan Cho, Jeong Gon Son, and Bongjun Yeom*

Cite This: *ACS Appl. Mater. Interfaces* 2021, 13, 54301−54307 Read Online

ACCESS | Metrics & More | Article Recommendations | Supporting Information

ABSTRACT: Research on the chiral magneto-optical properties of inorganic nanomaterials has enabled novel applications in advanced optical and electronic devices. However, the corresponding chiral magneto-optical responses have only been studied under strong magnetic fields of ≥1 T, which limits the wider application of these novel materials. In this paper, we report on the enhanced chiral magneto-optical activity of supra-assembled Fe_3O_4 magnetite nanoparticles in the visible range at weak magnetic fields of 1.5 mT. The spherical supra-assembled particles with a diameter of ∼90 nm prepared by solvothermal synthesis had single-crystal-like structures, which resulted from the oriented attachment of nanograins. They exhibited superparamagnetic behavior even with a relatively large supraparticle diameter that exceeded the size limit for superparamagnetism. This can be attributed to the small size of nanograins with a diameter of ∼12 nm that constitute the suprastructured particles. Magnetic circular dichroism (MCD) measurements at magnetic fields of 1.5 mT showed distinct chiral magneto-optical activity from charge transfer transitions of magnetite in the visible range. For the supraparticles with lower crystallinity, the MCD peaks in the 250−550 nm range assigned as the ligand-to-metal charge transfer (LMCT) and the inter-sublattice charge transfer (ISCT) show increased intensities in comparison to those with higher crystallinity samples. On the contrary, the higher crystallinity sample shows higher MCD intensities near 600−700 nm for the intervalence charge transfer (IVCT) transition. The differences in MCD responses can be attributed to the crystallinity determined by the reaction time, lattice distortion near grain boundaries of the constituent nanocrystals, and dipolar interactions in the supra-assembled structures.

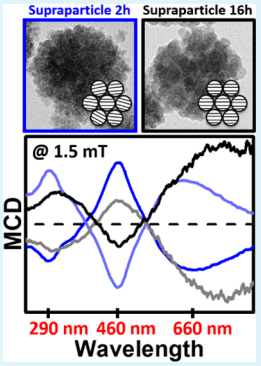

KEYWORDS: *chirality, magneto-optical property, magnetite, supra-assembly, magnetic circular dichroism*

INTRODUCTION

The assembly of inorganic nanoparticles into well-defined suprastructures is an important and state-of-the-art approach for the fabrication of advanced functional materials.[1,2] The specific multiparticle interactions in different suprastructures, manifested as collective properties, often result in unique and interesting optical phenomena compared to those observed in their individual nanoparticle counterparts. A few examples are plasmonic hybridization modes such as dark mode and fano resonances in assembled plasmonic molecules,[3,4] quantum coupling in assembled colloidal quantum dots,[5,6] and collective chiral optical activity of the ensembles of chiral assembled inorganic nanostructures.[7,8] In addition, the supra-nanostructures assembled by metal and metal-oxide materials can exhibit chiral magneto-optical properties, and owing to their potential applications in advanced optoelectronic devices[7,9] and nanomedicine,[10,11] they have been attracting increased attention. However, the chiral magneto-optical responses related to these assembled structures have not yet been fully understood.

The chiral magneto-optical activity indicates light−matter interaction with the preferential absorption of circularly polarized light (CPL) under an applied magnetic field parallel to the direction of light propagation.[12,13] This phenomenon arises from the absence of time-reversal and space-inversion symmetries in magnetized materials,[14] which are the main magneto-optical effects together with Faraday and Kerr effects.[15,16] Such preferential absorption under a magnetic field can be measured by magnetic circular dichroism (MCD) spectroscopy, which is highly suitable for determining the degeneracy of electronic energy levels and spin and oxidation states on molecular scales.[17−19] However, studies on the MCD response in nanoscale materials are still in the initial stages. Recently, Wu et al. demonstrated a 12-fold enhancement in the chiroptical response in $Au@Fe_3O_4$ core−satellite nanostructures in the presence of the magnetic field.[20] Yeom et al. showed that superparamagnetic Co_3O_4 nanoparticles with chiral distortions in the crystal lattice exhibit intense chiro-magneto-optical activity in the visible region, originating from the strong contribution of the magnetic transition dipole moment to the polarization rotation.[21] Lee and co-workers fabricated magnetoplasmonic graphene nanocomposites and

Received: September 3, 2021
Accepted: October 28, 2021
Published: November 8, 2021

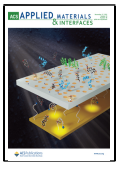

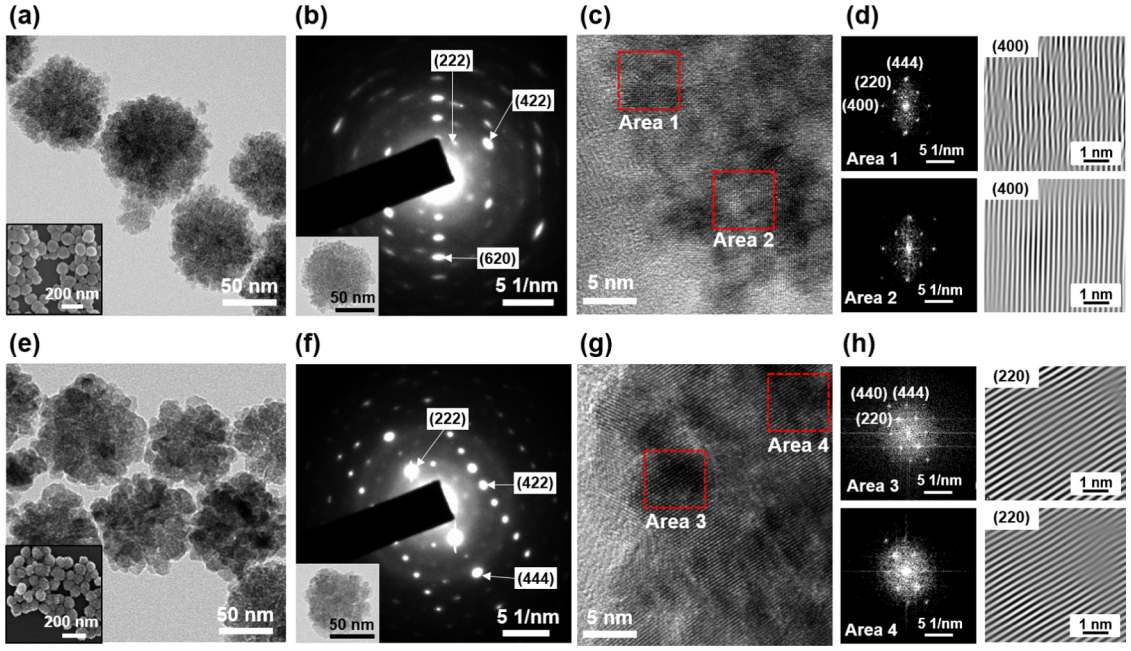

Figure 1. Electron microscopy analysis of (a–d) Fe_3O_4 supra-assembled particles with a reaction time of 2 h (SP1) and (e–h) Fe_3O_4 supra-assembled particles with a reaction time of 16 h (SP2). Transmission electron microscopy (TEM) images of (a, c) SP1 and (e, g) SP2. The insets at the bottom left corner of panels (a) and (e) show scanning electron microscopy (SEM) images of SP1 and SP2. (b, f) Selected-area diffraction (SAED) patterns for each sample. The insets show TEM images of the supraparticles used for the SAED analysis. (c, g) High-resolution TEM (HRTEM) images with selected regions indicated by red dotted boxes for fast Fourier transform (FFT) analysis. (d, h) FFT patterns from the selected areas. The inverse patterns of the (400) planes from Areas 1 and 2 are shown selectively in the right panel of (d) for convenient comparison of crystallographic orientations. (h) FFT patterns of Areas 3 and 4 from the (220) planes.

studied the magnetic and electron spin-derived magneto-optical activity using MCD.[22] Very recently, the same group demonstrated that the application of the helical magnetic field on Ag@Fe_3O_4 core–shell nanoparticles induces self-assembly to create optically active helical suprastructures in real time.[23] Han et al. reported that distinctly different MCD responses were registered by transverse and longitudinal surface plasmon resonances of gold nanorods, with the chiral magneto-optical response controlled by the geometry of the nanostructures.[24] However, the chiral magneto-optical activity of the nanostructures in the previous reports has only been observed under strong magnetic fields in the order of ≥1 T, and the number of studies at lower magnetic fields is limited, presumably due to the weak responses.

In this paper, we report on the chiral magneto-optical responses of supra-assembled magnetite (Fe_3O_4) nanoparticles (SPs) in the visible range under weak applied fields of 1.5 mT. SPs, prepared by a single-step solvothermal synthesis method, had spherical shapes of the ensemble of small nanograins with oriented attachment, mimicking the structures of biominerals. SPs, even with a relatively large diameter of ∼90 nm, exhibited superparamagnetic behavior. We additionally controlled the reaction times for SPs to impart different degrees of crystallinity in the supra-assembled structures. The resultant MCD spectra show distinct responses for each charge transfer that are attributed to crystallinity determined by the reaction time, lattice distortion near grain boundaries of the constituent nanocrystals, and dipolar interactions in the supra-assembled structures.

RESULTS AND DISCUSSION

SPs were prepared by a solvothermal method[25] with minor modifications in the synthesis protocol and the reaction times were adjusted as 2 h (denoted as SP1) and 16 h (denoted as SP2) (for details of the synthesis, see the Experimental Methods section and scheme of Figure S1). The transmission electron microscopy (TEM) images in Figure 1a,e reveal that both samples have spheroidal shape, where each supraparticle is composed of densely packed smaller individual nanocrystals. As shown in the scanning electron microscopy (SEM) images in the insets at the lower corners in Figure 1a,e, most SPs have a similar size with large-scale uniformity (see additional images in Figure S2). The diameters of SP1 and SP2 are 93(2) and 92(4) nm, respectively, calculated from histogram analysis by fitting with log-normal distribution functions (Figure S2).[26,27] The selected-area electron diffraction (SAED) pattern obtained for SP1 exhibited a dot-like pattern with small streaks on the individual dots (Figure 1b), which is a typical fingerprint for a single-crystal-like arrangement of the nanocrystal domains in the SP.[28,29] The spots in the diffraction pattern were assigned to the (222), (422), and (620) lattice fringes of a cubic inverse spinel structure of magnetite.[30] On the other hand, the SAED pattern for SP2 (Figure 1f) shows higher reflection of the lattice fringes with more or less ellipsoidal-shaped dot patterns. This indicates that SP2 with a longer reaction time has higher degree of the aligned nanocrystals that is more close to the single-crystal structure than SP1. This is coincident with the observation of apparently larger nanocrystal domains comprising SP2 (Figure 1e) than those in SP1 (Figure 1a).

Figure 1c shows a high-resolution TEM (HRTEM) image of the edge of SP1, and the results of the fast Fourier transform (FFT) analysis for the red dotted boxes in the HRTEM image are shown in Figure 1d. Areas 1 and 2 in Figure 1c were arbitrarily chosen to compare the orientation of the crystal lattices at different locations in SP1. Among the lattice planes

https://doi.org/10.1021/acsami.1c16954
ACS Appl. Mater. Interfaces 2021, 13, 54301–54307

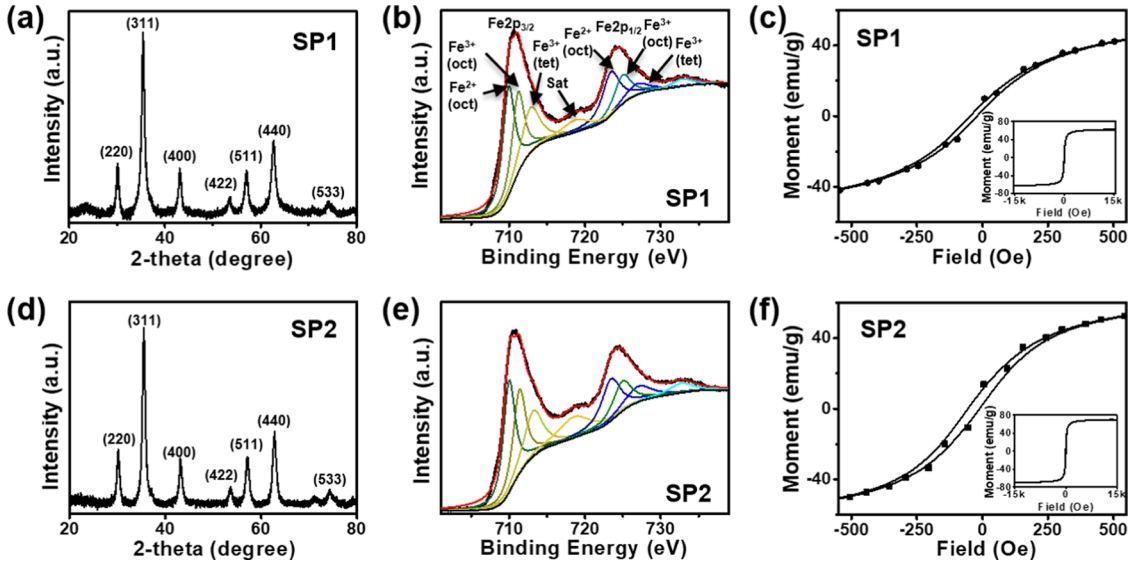

Figure 2. X-ray diffraction (XRD) spectra for (a) SP1 and (d) SP2. The peaks are indexed to pure magnetite (JCPDS No. 85-1436). Fe 2p X-ray photoelectron spectra (XPS) of (b) SP1 and (e) SP2, including the deconvoluted spectra and summarized fitting results. Room-temperature magnetization curves for (c) SP1 and (f) SP2. To show the saturations, the full magnetization range is provided in the insets.

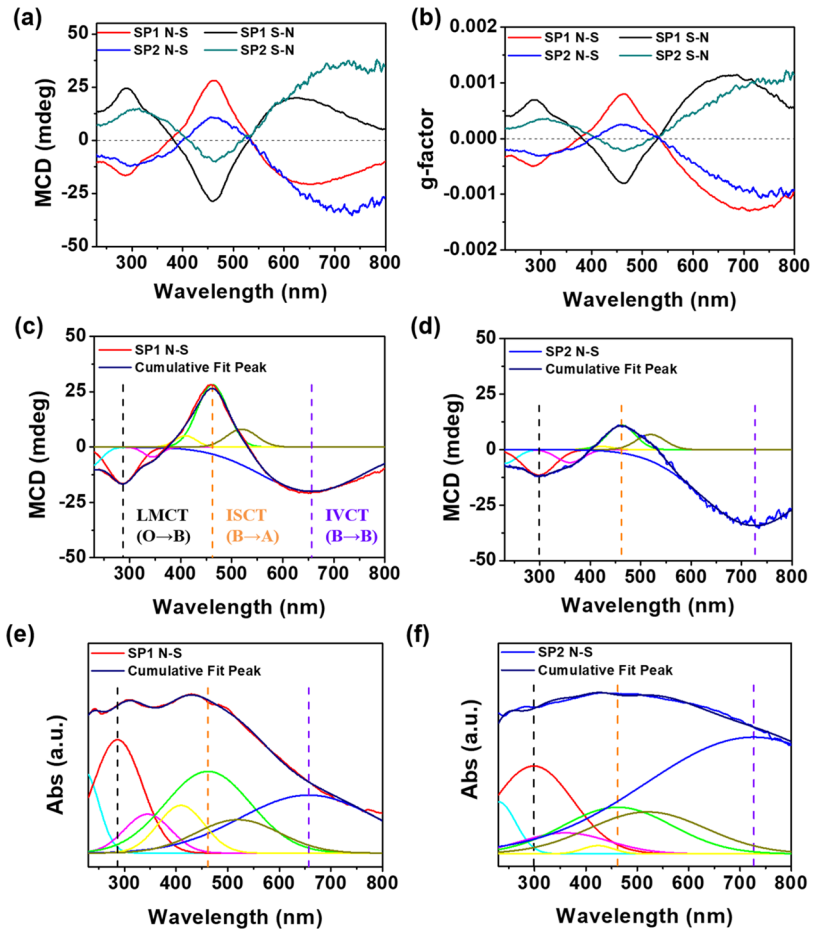

Figure 3. Chiral magneto-optical properties of SP1 and SP2 under an applied magnetic field of 1.5 mT. (a) Magnetic circular dichroism (MCD), (b) *g*-factor, (c, d) deconvolution of MCD spectra, and (e, f) ultraviolet−visible (UV−vis) absorbance spectra.

indexed in the FFT pattern shown in Figure 1d, the (400) lattice planes were inversely transformed, as shown in the right panel of Figure 1d for convenient comparison of the crystallographic orientation between Areas 1 and 2. The angle between the orientated lattice planes was measured to be only about 1.9°. In the same analysis for SP2, the (220) lattice planes from Areas 3 and 4 show less degree of orientation angle about 1.0° (Figure 1g,h). These alignments among the

https://doi.org/10.1021/acsami.1c16954
ACS Appl. Mater. Interfaces 2021, 13, 54301−54307

nanocrystal domains are in agreement with the result of the single-crystal-like SAED patterns, which confirms that SP2s are formed in greater alignment of orientations than SP1s.[31] Different from the aqueous media-based synthesis methods, for the solvothermal methods with ethylene glycol, it was reported that the nucleation, growth, and assembly of the smaller individual nanocrystals occurred at a kinetically slower rate owing to the availability of very few surface hydroxyls as well as due to the high viscosity of ethylene glycol.[31,32] Longer reaction time could further promote their rotation sufficiently to locate low-energy interfaces and share common crystallographic orientation in the supra-assembled structures (schematic illustration in Figure S1).[33]

Powder X-ray diffraction (XRD) measurements were conducted. Both the SPs show distinct reflections of fcc magnetite (JCPDS No. 85-1436) indexed with (220), (311), (400), (422), (511), (440), and (533) peaks (Figure 2a,d). The mean crystal sizes obtained using the Scherrer equation[34] were 11.8 and 12.2 nm for the SP1 and SP2 samples, respectively. These sizes are significantly smaller than the overall size of the individual SPs, ∼90 nm, which further support the oriented attachment of the smaller nanocrystal domains to form SPs.

X-ray photoelectron spectra (XPS) of the SP samples consist of a doublet of Fe $2p_{3/2}$ and Fe $2p_{1/2}$ peaks. The best fits were obtained using deconvolution for elements corresponding to Fe^{2+} (octahedral), Fe^{3+} (octahedral), and Fe^{3+} (tetrahedral). The satellite peaks were in good agreement with previous reports for magnetite (Figure 2b,e).[35,36] The fitting parameters obtained after deconvolution, including the peak positions, full width at half-maximum (FWHM) values, and peak areas are listed in Tables S1 and S2. The $2p_{3/2}/2p_{1/2}$ peak area ratios were calculated as 2.1 and 2.0 for SP1 and SP2, respectively, and which were similar to their anticipated value of 2 for magnetite.[37] The Fe^{2+}/Fe^{3+} ratios calculated from the Fe $2p_{3/2}$ peak were determined to be 0.73 and 0.68 for SP1 and SP2, respectively. The reported values for the Fe^{2+}/Fe^{3+} ratio from various types of magnetite varied from 0.45 to 0.77 (theoretical number 0.5).[36−38] Reduction from high vacuum conditions in the XPS measurement was referred for the higher ratio case.[36]

The field-dependent magnetization measurements in a wide range of magnetic fields from −15 to 15 kOe revealed that both SPs exhibit superparamagnetic behavior (insets in Figure 2c,f).[39,40] The saturation magnetization (M_s) values were 62 and 70 emu/g for SP1 and SP2, respectively. The difference in the saturation magnetization value from bulk magnetite can be attributed to the existence of spin disorder, which is due to the defects in the coordination environment at the surfaces and interfaces of the nanocrystal domains for SPs.[41] The lower degree of crystallinity with more interfaces for SP1 can be attributed to the lower M_s values compared to those for SP1. For the scanning region from −500 to 500 Oe shown in Figure 2c,f, SP1 exhibited a smaller magnitude of hysteresis compared to that of SP2, which supports previous observations for smaller sizes of nanocrystal domains for SP1.

We studied the chiral magneto-optical activity of SPs by MCD measurements under weak fields of 1.5 mT (Figure 3). MCD shows absorption difference of left-handed and right-handed CPLs under magnetic fields. It is utilized to examine spin-split valence electronic structures.[15,20,42] The magnetic field can induce polarized electronic states for optical transition of magnetite, which show preferential absorptions of CPLs. Without application of the magnetic field, SP samples showed traces of CD signals at the region of 500−700 nm (Figure S3). However, CD signals disappeared with vigorous agitations (Figure S4), indicating that these CD signals originated from anisotropic interferences by partial adsorption or precipitation of the samples.[43] To interpret the contribution of the corresponding charge transfer transitions for spectral changes in the MCD spectra, both the MCD and absorbance spectra were deconvoluted using a seven-band description with Gaussian distributions.[15,20] The dotted lines shown in Figure 3c,d indicate the positions of the major charge transfer deconvoluted peaks in the MCD spectra and the UV−vis absorbance data shown in Figure 3e,f.[42] For the fitting of each sample data, the same positions of deconvoluted peaks are utilized for both the MCD and UV−vis absorbance, while widths and amplitudes are adjusted for best-fitting results. Additional information on the deconvolution and peak assignments are shown in Table S3. Optical transitions are assigned based on the previous study.[42] B indicates Fe^{2+} and Fe^{3+} at the octahedral sites and A indicates Fe^{3+} at the tetrahedral sites. By applying the magnetic field, the MCD spectra of both the SPs exhibited distinct shapes with multiple peaks in modulation, while mirrored shapes of MCD spectra were observed upon changing the direction of the magnetic field from N−S to S−N. This indicates that the application of an external magnetic field induces preferential spin polarization with respect to the direction of the applied field in SPs[15,22] and manifests itself as spin-dependent chiral magneto-optical activity. N−S magnetic configurations were only utilized for the interpretation of the deconvoluted MCD spectra, and positive and negative deconvoluted peaks are assigned to optical transitions for spin majority (↑) and minority (↓), respectively.[42]

Specifically, the MCD spectra and *g*-factors of SP1 show stronger chiral magneto-optical properties in the range of 250−500 nm than those of SP2, as shown in Figure 3a,b. For the SP1 sample (Figure 3c,e), three deconvoluted peaks at 222.5, 287.0, and 345.0 nm were assigned to the ligand-to-metal charge transfer (LMCT) transitions of $O(2p)\downarrow \rightarrow B(t_{2g})\downarrow$. The positive strong peak at 462.1 nm with additional weak positive peaks at 410.0 and 519.9 nm can be attributed to the inter-sublattice charge transfer (ISCT) transitions of $B(e_g)\uparrow \rightarrow A(e_g;t_{2g})\uparrow$. On the other hand, the SP2 sample shows stronger MCD responses and similar *g*-factor values in the 600−800 nm region in comparison to the SP1 sample, which can be mainly attributed to the intervalence charge transfer (IVCT) transition, $B(t_{2g})\downarrow \rightarrow B(e_g)\downarrow$. For the same IVCT transition, the UV−vis absorbance peak area for the SP2 sample shows a greater peak area of 40.2% than that for the SP1 sample, 26.7% (Figure 3e,f and Table S3).

Stronger MCD intensity in IVCT transitions for SP2, in comparison with other transitions, can be attributed to increased crystallinity from prolonged reactions, lattice distortion near nanograin boundaries, and dipolar couplings of the constituent nanocrystals in the supra-assembled structure. When magnetite crystals start to grow from Fe^{3+} ions, the additional UV−vis absorbances at the higher wavelength region gradually appear by the formation of reaction intermediates of $Fe(OH)_3$ and $Fe(OH)_2$.[44,45] Similar results were obtained from the reactants and the initial stage of reactions (Figures S4 and S5). Since SP2 was synthesized with a longer reaction time of 16 h, it contains higher degree of crystallinity and lower proportion of the disordered coordinating environment at the surfaces and interfaces. This may

https://doi.org/10.1021/acsami.1c16954
ACS Appl. Mater. Interfaces 2021, 13, 54301−54307

enable the direct electron hopping transfer between Fe^{2+} and Fe^{3+} at the octahedral sites of the IVCT transition that is easier than the case for SP1 with lower crystallinity.[46] Additionally, we can still observe ellipsoidal-shaped dots in the SAED patterns of Figure 1f. This indicates that some degree of crystallographic mismatch exists at the grain boundaries of the constituent nanocrystals, deviating from the single crystal. This is also consistent with XRD results that the crystal size of SP2 is still much smaller than the size of the supraparticle (Figure 2d). Such strained conditions may lead to lattice distortion in the vicinity of the boundaries, and it can contribute to the relaxation of Laporte selection for optical transitions of octahedral complexes.[42,47] Furthermore, MCD signals for the suprastructures were greater than the magnetite nanoparticles synthesized by the coprecipitation method (Figure S6).[48] This can be attributed to dipolar coupling between the magnetic moments of the individual constituent nanocrystals, which can actively respond even under a small magnetic field of 1.5 mT due to their superparamagnetic properties.

CONCLUSIONS

In conclusion, we presented the chiral magneto-optical activity of magnetite supraparticles prepared by a modified solvothermal method with different reaction times. The supra-assembled magnetite particles exhibited chiral magneto-optical activity even under weak applied fields of 1.5 mT. The distinct peaks obtained were attributed to IVCT, ISCT, and LMCT transitions of magnetite. SP1 with a shorter reaction time and lower crystallinity shows greater chiral magneto-optical responses in the visible range of 250−500 nm, attributed to LMCT and ISCT than SP2 with a longer reaction time and higher crystallinity. On the other hand, higher MCD intensities from IVCT were observed at the higher wavelength region >600 nm for SP2 than those of SP1. Differences in the MCD responses are attributed to the degree of crystallization, existence of lattice distortion, and dipolar coupling from the supra-assembled structures with superparamagnetic properties. This work can contribute to a deeper understanding of the magneto-optical activities of magnetic nanomaterials for advanced optical and electronic applications.

EXPERIMENTAL METHODS

Materials. $FeCl_3{\cdot}6H_2O$, $FeSO_4{\cdot}7H_2O$, ethylene glycol, Tween 20, sodium acetate, and ammonia solution (30%) were obtained from Sigma-Aldrich and used as received. All chemicals used in our synthetic methods were of analytical-grade purity. Before use, all glassware and Teflon products were thoroughly cleaned with aqua regia.

Synthesis of Magnetite Supraparticles (SPs). The synthesis of SPs was carried out according to the procedure reported by Maqbool et al. with minor modifications.[25] $FeCl_3{\cdot}6H_2O$ (135.15 mg, 0.5 mmol) was dissolved in 4 mL of ethylene glycol in a 15-mL-capacity screw-top tube, followed by the addition of CH_3COONa (360 mg, 4.39 mmol), 10 μL of Tween 20, and 200 μL of ultrapure water. The obtained yellow reaction mixture was stirred at room temperature for 30 min at a stirring rate of 400 rpm. At this point, the screw-top tube was sealed and transferred into an oil bath preheated to 200 °C. The reaction mixture was simultaneously heated (at 200 °C), stirred (at 375 rpm) for 2 or 16 h, and then naturally cooled to room temperature. After the stirring was stopped, the obtained black precipitate was attached to the magnetic bead with a clear, transparent supernatant. This magnetic precipitate was washed five times with ethanol using a magnet and dried in a hot air oven at 55 °C for 6 h.

Synthesis of Magnetite Nanoparticles (NPs). The synthesis of NPs was carried out using the coprecipitation method.[48] First, 2 mmol of $FeCl_3{\cdot}6H_2O$ and 1 mmol of $FeSO_4{\cdot}7H_2O$ (each compound was dissolved in 15 mL of ultrapure water) were mixed in a 50 mL round-bottom flask for 30 min at room temperature with a stirring rate of 500 rpm. Subsequently, this metal ion solution was transferred into an oil bath preheated to 90 °C and heated at this temperature for 10 min at a stirring rate of 500 rpm. Then, 5 mL of aqueous ammonia solution (30%) was added drop-wise to the hot metal ion solution using a syringe. The obtained black colloidal solution was stirred (at 500 rpm) at 90 °C for 1 h and subsequently allowed to cool to room temperature naturally. The obtained black product was washed five times with ethanol using a magnet and dried in an oven at 55 °C for 6 h.

Characterization. Powder X-ray diffraction (XRD) patterns were obtained using a diffractometer (X'Pert Pro, Malvern Panalytical B.V., The Netherlands) equipped with Cu Kα (λ = 1.54 Å) incident X-rays as the irradiation source, and the diffraction data were collected in a 2θ range of 10−80°. For each sample, the mean crystal domain size was obtained using the Scherrer equation for the major diffraction peak (311). X-ray photoelectron spectra (XPS) were recorded on an X-ray photoelectron spectrometer system (K-Alpha, Thermo Fisher Scientific Inc.) with binding energies obtained with reference to the C 1s peak (284.8 eV) of adventitious carbon. The morphology of the samples was analyzed using a field-emission scanning electron microscope (FESEM, S-4800, Hitachi High-Tech Corporation, Japan) operated at an acceleration voltage of 5 kV. Approximately 20 μL of colloidal suspension of the samples in ethanol (concentration 0.05 mg/mL) was drop-casted on a freshly cleaned silicon wafer held under ambient conditions for 30 min and then dried in an oven at 50 °C for 12 h. This silicon wafer containing the sample was attached to a conductive carbon tape and coated with platinum by sputter coating for 30 s before visualization by SEM. The internal structure of the samples was analyzed by transmission electron microscopy (TEM, JEM-2100F, JEOL Ltd., Japan) operated at an acceleration voltage of 200 kV. For the sample preparation, 10 μL of colloidal suspensions of the samples in ethanol (concentration 0.05 mg/mL) were drop-casted on a carbon-coated copper grid and held for 30 min at room temperature to evaporate the solvent. The magnetic properties of the samples were obtained using a vibrating sample magnetometer (VSM, Lake Shore Cryotronics, Inc.) using preweighed amounts of dry powder samples enclosed in gelatin capsules. The saturation magnetization curves were obtained using a maximum applied magnetic field of ±15 kOe at 298 K.

Magnetic Circular Dichroism (MCD) Measurements. All MCD experiments were performed on dilute colloids (0.1 mg/mL) in ethylene glycol using quartz cuvettes with a path length of 1 cm, under ambient conditions. For each sample, the ultraviolet−visible (UV−vis) and MCD spectra were recorded using a spectrometer (J-1500 CD, JASCO, Inc.) in the wavelength range of 200−800 nm. We controlled the weak applied magnetic fields (1.5 mT) using a neodymium magnet. The g-factor was calculated from the collected UV−vis and MCD values.

ASSOCIATED CONTENT

Supporting Information

The Supporting Information is available free of charge at https://pubs.acs.org/doi/10.1021/acsami.1c16954.

XPS and UV−vis tables for deconvolution, schematic illustration, additional SEM and TEM images, and MCD spectra for the nanoparticles (PDF)

AUTHOR INFORMATION

Corresponding Author

Bongjun Yeom − *Department of Chemical Engineering, Hanyang University, Seoul 04763, Republic of Korea;* orcid.org/0000-0001-8914-0947; Email: byeom@hanyang.ac.kr

Authors

Qysar Maqbool − *Department of Chemical Engineering and Institute of Nano Science and Technology, Hanyang University, Seoul 04763, Republic of Korea*

Arum Jung − *Department of Chemical Engineering, Hanyang University, Seoul 04763, Republic of Korea*

Sojeong Won − *Department of Chemical Engineering, Hanyang University, Seoul 04763, Republic of Korea*

Jinhan Cho − *Department of Chemical and Biological Engineering and KU-KIST Graduate School of Converging Science and Technology, Korea University, Seoul 02841, Republic of Korea;* orcid.org/0000-0002-7097-5968

Jeong Gon Son − *KU-KIST Graduate School of Converging Science and Technology, Korea University, Seoul 02841, Republic of Korea; Soft Hybrid Materials Research Center, Korea Institute of Science and Technology (KIST), Seoul 02792, Republic of Korea;* orcid.org/0000-0003-3473-446X

Complete contact information is available at: https://pubs.acs.org/10.1021/acsami.1c16954

Author Contributions

[⊥]Q.M. and A.J. contributed equally to this work.

Notes

The authors declare no competing financial interest.

■ ACKNOWLEDGMENTS

The authors acknowledge financial support from the National Research Foundation of Korea (NRF) grant funded by the Korea Government (Ministry of Science and ICT) (Nos. NRF-2021R1A2C4002523 and NRF-2019R1A4A1027627) and the Korea Institute of Science and Technology (KIST) Institutional Program (Project No. 2V08210). This work was supported by the Korea Institute of Energy Technology Evaluation and Planning (KETEP) and the Ministry of Trade, Industry & Energy (MOTIE) of the Republic of Korea (No. 20202020800330).

■ REFERENCES

(1) Xu, L.; Ma, W.; Wang, L.; Xu, C.; Kuang, H.; Kotov, N. A. Nanoparticle Assemblies: Dimensional Transformation of Nanomaterials and Scalability. *Chem. Soc. Rev.* **2013**, *42*, 3114−3126.

(2) Auyeung, E.; Li, T. I. N. G.; Senesi, A. J.; Schmucker, A. L.; Pals, B. C.; de la Cruz, M. O.; Mirkin, C. A. DNA-Mediated Nanoparticle Crystallization into Wulff Polyhedra. *Nature* **2014**, *505*, 73−77.

(3) Sancho-Parramon, J.; Bosch, S. Dark Modes and Fano Resonances in Plasmonic Clusters Excited by Cylindrical Vector Beams. *ACS Nano* **2012**, *6*, 8415−8423.

(4) Yi, C.; Dongare, P. D.; Su, M.-N.; Wang, W.; Chakraborty, D.; Wen, F.; Chang, W.-S.; Sader, J. E.; Nordlander, P.; Halas, N. J.; Link, S. Vibrational Coupling in Plasmonic Molecules. *Proc. Natl. Acad. Sci. U.S.A.* **2017**, *114*, 11621−11626.

(5) Cui, J.; Panfil, Y. E.; Koley, S.; Shamalia, D.; Waiskopf, N.; Remennik, S.; Popov, I.; Oded, M.; Banin, U. Colloidal Quantum Dot Molecules Manifesting Quantum Coupling at Room Temperature. *Nat. Commun.* **2019**, *10*, No. 5401.

(6) Koley, S.; Cui, J.; Panfil, Y. E.; Banin, U. Coupled Colloidal Quantum Dot Molecules. *Acc. Chem. Res.* **2021**, *54*, 1178−1188.

(7) Fan, J.; Kotov, N. A. Chiral Nanoceramics. *Adv. Mater.* **2020**, *32*, No. 1906738.

(8) Zhang, Q.; Hernandez, T.; Smith, K. W.; Jebeli, S. A. H.; Dai, A. X.; Warning, L.; Baiyasi, R.; McCarthy, L. A.; Guo, H.; Chen, D.-H.; Dionne, J. A.; Landes, C. F.; Link, S. Unraveling the Origin of Chirality from Plasmonic Nanoparticle-Protein Complexes. *Science* **2019**, *365*, 1475−1478.

(9) Oh, S. S.; Hess, O. Chiral metamaterials: enhancement and control of optical activity and circular dichroism. *Nano Convergence* **2015**, *2*, No. 24.

(10) Yeom, J.; Guimaraes, P. P. G.; Ahn, H. M.; Jung, B.-K.; Hu, Q.; McHugh, K.; Mitchell, M. J.; Yun, C.-O.; Langer, R.; Jaklenec, A. Chiral Supraparticles for Controllable Nanomedicine. *Adv. Mater.* **2020**, *32*, No. 1903878.

(11) Thimiri Govinda Raj, D. B.; Khan, N. A. Surface functionalization dependent subcellular localization of Superparamagnetic nanoparticle in plasma membrane and endosome. *Nano Convergence* **2018**, *5*, No. 4.

(12) Stephens, P. J. Theory of Magnetic Circular Dichroism. *J. Chem. Phys.* **1970**, *52*, 3489−3516.

(13) Han, B.; Gao, X.; Lv, J.; Tang, Z. Magnetic Circular Dichroism in Nanomaterials: New Opportunity in Understanding and Modulation of Excitonic and Plasmonic Resonances. *Adv. Mater.* **2020**, *32*, No. 1801491.

(14) Christofi, A. Strong Magnetochiral Dichroism in Chiral/Magnetic Layered Heterostructures. *Opt. Lett.* **2018**, *43*, 5741−5744.

(15) Yao, H.; Ishikawa, Y. Finite Size Effect on Magneto-Optical Responses of Chemically Modified Fe_3O_4 Nanoparticles Studied by MCD Spectroscopy. *J. Phys. Chem. C* **2015**, *119*, 13224−13230.

(16) Lodewijks, K.; Maccaferri, N.; Pakizeh, T.; Dumas, R. K.; Zubritskaya, I.; Åkerman, J.; Vavassori, P.; Dmitriev, A. Magneto-plasmonic Design Rules for Active Magneto-Optics. *Nano Lett.* **2014**, *14*, 7207−7214.

(17) Kobayashi, N.; Nakai, K. Applications of Magnetic Circular Dichroism Spectroscopy to Porphyrins and Phthalocyanines. *Chem. Commun.* **2007**, *40*, 4077−4092.

(18) Bradley, J. M.; Silkstone, G.; Wilson, M. T.; Cheesman, M. R.; Butt, J. N. Probing a Complex of Cytochrome c and Cardiolipin by Magnetic Circular Dichroism Spectroscopy: Implications for the Initial Events in Apoptosis. *J. Am. Chem. Soc.* **2011**, *133*, 19676−19679.

(19) Wang, Z.; Tavabi, A. H.; Jin, L.; Rusz, J.; Tyutyunnikov, D.; Jiang, H.; Moritomo, Y.; Mayer, J.; Dunin-Borkowski, R. E.; Yu, R.; Zhu, J.; Zhong, X. Atomic Scale Imaging of Magnetic Circular Dichroism by Achromatic Electron Microscopy. *Nat. Mater.* **2018**, *17*, 221−225.

(20) Wu, X.; Hao, C.; Xu, L.; Kuang, H.; Xu, C. Chiromagnetic Plasmonic Nanoassemblies with Magnetic Field Modulated Chiral Activity. *Small* **2020**, *16*, No. 1905734.

(21) Yeom, J.; Santos, U. S.; Chekini, M.; Cha, M.; Moura, A. F.; de Kotov, N. A. Chiromagnetic Nanoparticles and Gels. *Science* **2018**, *359*, 309−314.

(22) Lee, J.; Lee, J. Magneto-Optically Active Magnetoplasmonic Graphene. *Chem. Commun.* **2017**, *53*, 5814−5817.

(23) Jeong, K.-J.; Lee, D. K.; Tran, V. T.; Wang, C.; Lv, J.; Park, J.; Tang, Z.; Lee, J. Helical Magnetic Field-Induced Real-Time Plasmonic Chirality Modulation. *ACS Nano* **2020**, *14*, 7152−7160.

(24) Han, B.; Gao, X.; Shi, L.; Zheng, Y.; Hou, K.; Lv, J.; Guo, J.; Zhang, W.; Tang, Z. Geometry-Modulated Magnetoplasmonic Optical Activity of Au Nanorod-Based Nanostructures. *Nano Lett.* **2017**, *17*, 6083−6089.

(25) Maqbool, Q.; Singh, C.; Paul, A.; Srivastava, A. Uniform Spheroidal Nanoassemblies of Magnetite Using Tween Surfactants: Influence of Surfactant Structure on the Morphology and Electrochemical Performance. *J. Mater. Chem. C* **2015**, *3*, 1610−1618.

(26) Sturges, H. A. The Choice of a Class Interval. *J. Am. Stat. Assoc.* **1926**, *21*, 65−66.

(27) Aragón, F. H.; Coaquira, J. A. H.; Villegas-Lelovsky, L.; Da Silva, S. W.; Cesar, D. F.; Nagamine, L. C. C. M.; Cohen, R.; Menéndez-Proupin, E.; Morais, P. C. Evolution of the Doping Regimes in the Al-Doped SnO_2 Nanoparticles Prepared by a Polymer Precursor Method. *J. Phys.: Condens. Matter* **2015**, *27*, No. 095301.

(28) Liu, B.; Zeng, H. C. Mesoscale Organization of CuO Nanoribbons: Formation of "Dandelions.". *J. Am. Chem. Soc.* **2004**, *126*, 8124−8125.
(29) He, T.; Chen, D.; Jiao, X. Controlled Synthesis of Co_3O_4 Nanoparticles through Oriented Aggregation. *Chem. Mater.* **2004**, *16*, 737−743.
(30) Cavelius, C.; Moh, K.; Mathur, S. Chemically Designed Growth of Monodisperse Iron Oxide Nanocrystals. *Cryst. Growth Des.* **2012**, *12*, 5948−5955.
(31) Chen, Y.; Xia, H.; Lu, L.; Xue, J. Synthesis of Porous Hollow Fe_3O_4 Beads and Their Applications in Lithium Ion Batteries. *J. Mater. Chem.* **2012**, *22*, 5006−5012.
(32) Yu, D.; Sun, X.; Zou, J.; Wang, Z.; Wang, F.; Tang, K. Oriented Assembly of Fe_3O_4 Nanoparticles into Monodisperse Hollow Single-Crystal Microspheres. *J. Phys. Chem. B* **2006**, *110*, 21667−21671.
(33) Alivisatos, A. P. Naturally Aligned Nanocrystals. *Science* **2000**, *289*, 736−737.
(34) Patterson, A. L. The Scherrer Formula for X-Ray Particle Size Determination. *Phys. Rev.* **1939**, *56*, 978−982.
(35) Poulin, S.; França, R.; Moreau-Bélanger, L.; Sacher, E. Confirmation of X-Ray Photoelectron Spectroscopy Peak Attributions of Nanoparticulate Iron Oxides, Using Symmetric Peak Component Line Shapes. *J. Phys. Chem. C* **2010**, *114*, 10711−10718.
(36) Wilson, D.; Langell, M. A. XPS Analysis of Oleylamine/Oleic Acid Capped Fe_3O_4 Nanoparticles as a Function of Temperature. *Appl. Surf. Sci.* **2014**, *303*, 6−13.
(37) Vasilescu, C.; Latikka, M.; Knudsen, K. D.; Garamus, V. M.; Socoliuc, V.; Turcu, R.; Tombácz, E.; Susan-Resiga, D.; Ras, R. H. A.; Vékás, L. High Concentration Aqueous Magnetic Fluids: Structure, Colloidal Stability, Magnetic and Flow Properties. *Soft Matter* **2018**, *14*, 6648−6666.
(38) Grosvenor, A. P.; Kobe, B. A.; Biesinger, M. C.; McIntyre, N. S. Investigation of Multiplet Splitting of Fe 2p XPS Spectra and Bonding in Iron Compounds. *Surf. Interface Anal.* **2004**, *36*, 1564−1574.
(39) Tan, Y.; Zhuang, Z.; Peng, Q.; Li, Y. Room-Temperature Soft Magnetic Iron Oxide Nanocrystals: Synthesis, Characterization, and Size-Dependent Magnetic Properties. *Chem. Mater.* **2008**, *20*, 5029−5034.
(40) Zhang, L.; Wu, J.; Liao, H.; Hou, Y.; Gao, S. Octahedral Fe_3O_4 nanoparticles and Their Assembled Structures. *Chem. Commun.* **2009**, *29*, 4378−4380.
(41) Lian, J.; Anggara, K.; Lin, M.; Chan, Y. Formation of Hollow Iron Oxide Tetrapods via a Shape-Preserving Nanoscale Kirkendall Effect. *Small* **2014**, *10*, 667−673.
(42) Chen, J.; Hsu, H.-S.; Huang, Y.-H.; Huang, D.-J. Spin-Dependent Optical Charge Transfer in Magnetite from Transmitting Optical Magnetic Circular Dichroism. *Phys. Rev. B* **2018**, *98*, No. 085141.
(43) Yeom, J.; Yeom, B.; Chan, H.; Smith, K. W.; Dominguez-Medina, S.; Bahng, J. H.; Zhao, G.; Chang, W. S.; Chang, S. J.; Chuvilin, A.; Melnikau, D.; Rogach, A. L.; Zhang, P.; Link, S.; Kral, P.; Kotov, N. A. Chiral Templating of Self-Assembling Nanostructures by Circularly Polarized Light. *Nat. Mater.* **2015**, *14*, 66−72.
(44) Lopes, L.; de Laat, J.; Legube, B. Charge Transfer of Iron (III) Monomeric and Oligomeric Aqua Hydroxo Complexes: Semi-empirical Investigation into Photoactivity. *Inorg. Chem.* **2002**, *41*, 2505−2517.
(45) He, Q.; Liu, J.; Liang, J.; Liu, X.; Ding, Z.; Tuo, D.; Li, W. Sodium Acetate Orientated Hollow/Mesoporous Magnetite Nanoparticles: Facile Synthesis, Characterization and Formation Mechanism. *Appl. Sci.* **2018**, *8*, No. 292.
(46) Cuenca, J. A.; Bugler, K.; Taylor, S.; Morgan, D.; Williams, P.; Bauer, J.; Porch, A. Study of the Magnetite to Maghemite Transition Using Microwave Permittivity and Permeability Measurements. *J. Phys.: Condens. Matter* **2016**, *28*, No. 106002.
(47) Barnakov, Y. A.; Scott, B. L.; Golub, V.; Kelly, L.; Reddy, V.; Stokes, K. L. Spectral Dependence of Faraday Rotation in Magnetite-Polymer Nanocomposites. *J. Phys. Chem. Solids* **2004**, *65*, 1005−1010.
(48) Ahn, T.; Kim, J. H.; Yang, H.-M.; Lee, J. W.; Kim, J.-D. Formation Pathways of Magnetite Nanoparticles by Coprecipitation Method. *J. Phys. Chem. C* **2012**, *116*, 6069−6076.

https://doi.org/10.1021/acsami.1c16954
ACS Appl. Mater. Interfaces 2021, 13, 54301−54307